https://dx.doi.org/10.1016/j.nanoen.2022.107395.
This is the Pre-Published Version.

In-Situ Forming Lithiophilic-Lithiophobic Gradient Interphases for Dendrite-Free All-Solid-State Li Metal Batteries

Yanke Lin [a,1], Tianshuai Wang [a,1], Leicheng Zhang [a], Xudong Peng [a], Baoling Huang [a], Maochun Wu [c,*], Tianshou Zhao [a,b,**]

[a] *Department of Mechanical and Aerospace Engineering, The Hong Kong University of Science and Technology, Clear Water Bay, Kowloon, Hong Kong SAR, China*

[b] *Department of Mechanical and Energy Engineering, Southern University of Science and Technology, Shenzhen, 518055, China*

[c] *Department of Mechanical Engineering, The Hong Kong Polytechnic University, Hung Hom, Kowloon, Hong Kong SAR, China*

Abstract

Solid polymer electrolytes offer a promise for all-solid-state Li batteries due to their low cost and good processability. However, dendrites and the associated contact loss occurring at the undesirable Li/electrolyte interface during repeated plating and stripping remain a challenge. To address the issue, here, we propose to coat a thin layer containing Al/Li dual-salt onto the polyethylene oxide (PEO) electrolyte. When cycled with the Li metal anode, the salts are sequentially reduced, in-situ forming a lithiophilic Li-Al alloy-rich layer near the anode and a lithiophobic LiF-rich layer close to the electrolyte. The former improves the interfacial adhesion and regulate the Li nucleation, while the latter contributes to dendrite suppression due to its high interface energy against Li. As a result, the gradient interphase enables a Li/Li symmetrical cell to be stably cycled for over 1000 h without short circuits. Moreover, the full cell paired with the $LiFePO_4$ cathode shows enhanced cyclability, retaining 89.1% capacity after 350 cycles at 0.5 C. A pouch cell using the dual-salt coated electrolyte demonstrates a

[1] These authors contributed equally to this work.
[*] Corresponding author. E-mail: maochun.wu@polyu.edu.hk (M.C. Wu).
[**] Corresponding author. E-mail: zhaots@sustech.edu.cn (T.S. Zhao).

good performance and safety. This work provides a facile yet effective approach to construct functional interphase for achieving stable batteries using solid polymer electrolytes.

Keywords: All-solid-state battery; solid polymer electrolyte; Li metal anode; gradient interphase; interface stability

1. Introduction

The unprecedented trend toward decarbonization has triggered pressing demands for safer, longer-lasting batteries, which have fostered the development of technologies beyond Li-ion batteries (LIBs) [1,2]. Among them, Li metal batteries are regarded as an ultimate solution due to the ultrahigh specific capacity of the Li metal anode (3860 mAh g^{-1}), which is about ten times higher than that of conventional graphite anode (372 mAh g^{-1}) [3]. However, the implementation of Li metal anode is hindered by severe Li dendrite formation, which not only leads to rapid capacity decay but also poses short circuit-induced safety concerns in the presence of flammable liquid electrolytes [4,5].

Replacing combustible liquid electrolytes with non-flammable solid electrolytes represents an effective approach to address the safety issues and potentially allows the use of Li metal anode for achieving energy-dense batteries [6,7]. Thus, all-solid-state Li batteries (ASSLBs) have attracted considerable attention from both academia and industry in recent years [8–13]. These efforts have led to the discovery of a wide variety of solid electrolytes, of which solid polymer electrolytes (SPEs) are one of the most promising candidates for practical ASSLBs because of their low cost, flexibility, and readiness for large-scale roll-to-roll fabrication [14–18]. Among various SPEs, PEO-based electrolytes are particularly attractive due to their decent ionic conductivity (10^{-5}~10^{-4} mS cm^{-1}) after incorporating Li salts such as lithium bis(trifluoromethanesulfonyl)imide (LiTFSI), compared to other polymers like polyvinylidene

fluoride (PVDF) and polyacrylonitrile (PAN) (10^{-6}~10^{-7} mS cm^{-1}) [19–22]. Moreover, the PEO electrolytes exhibit good compatibility with Li metal, leading to a relatively stable solid electrolyte interphase (SEI) after cycling with Li metal anode [23,24].

Unfortunately, the practical applications of SPEs are still hindered by severe Li dendrite formation that leads to rapid short circuits [21,25]. This can be ascribed to the following two reasons. First, compared to ceramic solid electrolytes, polymers usually exhibit insufficient mechanical strength for dendrite suppression. One approach to address this drawback is introducing an interlayer either with high modulus or lithiophobicity between the anode and the solid electrolyte [24,26–28]. For instance, Sun *et al.* developed a sandwich composite electrolyte with hierarchical garnet particles, wherein the surface layer facing the Li metal anode contains 80 vol% 5 μm garnet-type $Li_{6.4}La_3Zr_{1.4}Ta_{0.6}O_{12}$ particles to offer high strength for dendrite suppression [29]. Wang *et al.* demonstrated that a LiF-rich layer with high surface energy against Li could prevent the Li from penetrating into the solid electrolyte [30]. Unfortunately, these strategies would compromise the contact at the Li/PEO interface, which is the second issue [31,32]. Unlike liquid electrolytes which can spontaneously wet the electrodes, the morphology change of Li will lead to void formation and reduce the contact area at the anode/solid electrolyte interface, which will increase the local current density, consequently resulting in the growth of Li dendrite [31]. Bruce *et al.* used three-electrode cells to identify the critical stripping current of the sulfide solid electrolyte, and suggested that increasing stack pressure could effectively alleviate contact loss and increase the critical stripping current [31]. Accordingly, high stack pressure up to 250 MPa has been investigated as an effective approach to stabilize the anode interface in recent research [33]. Nevertheless, applying high stack pressure requires extra apparatus, which will complicate the system design and sacrifice the battery energy density, thus hindering their real-world applications [34]. Introducing lithiophilic coating, such as Pt [23], Ge [35], and Al_2O_3 [36], is another promising

approach to improve the contact at the Li/solid electrolyte interface [23,35]. However, this contradicts the wisdom that lithiophobicity is conducive to dendrite suppression [30,37]. Therefore, how to address the dilemma between lithiophilicity (good adhesion) and lithiophobicity (dendrite suppression) at the interface in a facile way remains a grand challenge for SPE-based Li batteries.

Here, to simultaneously alleviate the Li dendrite and contact loss during repeated plating/stripping processes, we propose to create an in-situ formed lithiophilic-lithiophobic gradient interphase, which is introduced by simply coating a layer containing aluminum trifluoromethanesulfonate ($Al(OTF)_3$)/LiTFSI dual-salt onto the PEO-based electrolyte. As schematically illustrated in Fig. 1a, in conventional PEO electrolyte with single Li salt, a LiF-rich SEI layer is formed by the reduction of Li salt at the Li/PEO interface during cycling [23,38]. Although LiF is widely regarded as a beneficial component for dendrite suppression [39,40], its lithiophobic nature would compromise the contact between the Li and PEO [41]. Consequently, the Li/PEO interface will become fluffy and porous upon cycling, resulting in uneven current density distribution and thus triggering Li dendrite formation. In contrast, after introducing the Al/Li dual-salt in the coating layer, the following reactions will preferably occur at the Li/PEO interface [42,43]:

$$3Li + Al^{3+} \rightarrow 3Li^{+} + Al \quad (1)$$

$$Al + xLi \rightarrow LixAl \quad (2)$$

The sequential reduction of Al^{3+} and anions will in-situ form lithiophilic-lithiophobic gradient interphase between Li metal and PEO electrolyte, as shown in Fig. 1b. The lithophilic Li-Al alloy-rich layer with lower interface energy against Li can enhance the adhesion between PEO and Li, thus reducing the interfacial resistance and alleviating the contact loss during cycling. Meanwhile, a lithiophobic LiF-rich layer will form above due to the reduction of anions, which will repel the dendrite growth due to its high interface energy against Li and electron-blocking

effect. As a consequence, the Li/Li symmetrical cell employing the coated electrolyte can be stably cycled for over 1000 h without short circuits. More remarkably, the Li/$LiFePO_4$ full battery is able to deliver a capacity of 149.2 mAh g^{-1} at 0.5 C with capacity retention of 89.1% after 350 cycles. In addition, the pouch cell exhibits a good performance and can even survive from blending and cutting, showing great promise for practical applications.

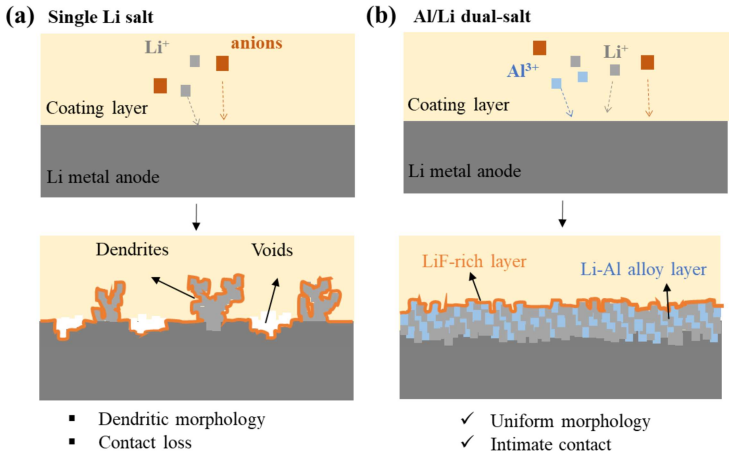

Fig. 1 Schematic illustration of the morphological evolution of Li/PEO interfaces with (a) single Li salt and (b) Al/Li dual-salt.

2. Results and discussion

2.1 Theoretical understanding of the lithiophilic-lithiophobic gradient interphase

Theoretical calculations based on density functional theory (DFT) were first performed to gain a fundamental understanding on how the components of the interphase function. Li_2Al was selected as the representative of Li-Al alloys in the SEI layer based on the ternary phase diagram of Li-Al-F (Fig. S1). At first, we calculated the interface energy of Li_2Al/Li and LiF/Li to identify the lithiophilic properties of Li_2Al and LiF (Note S1 and Fig. S2). Fig. 2a displays the relationship between the interface energy (γ) of two components and the number of Li metal formula units. Adopting the method reported by Holzwarth, the interface energy can be obtained from the intercept of the fitted line [44]. Results show that the Li_2Al/Li interface

exhibits a lower interface energy (10.10 meV A^{-2}) than that of the LiF/Li interface (48.11 meV A^{-2}), indicating the lithiophilicity of Li-Al alloys and lithiophobicity of the LiF. 2D cross-sectional charge density differences (inset in Fig. 2a) demonstrates that the superior lithiophilicity of Li-Al alloys is attributed to the more charge accumulation existing in the interface region. The lithiophilic nature of Li-Al alloy will enhance the interface contact and prevent the contact loss between Li and polymer electrolyte during repeated cycling.

Moreover, as the diffusivity of Li^+ can affect the Li initial nucleation and subsequent deposition processes, the diffusion of Li^+ between the two most stable adsorption sites on three surfaces was explored via the climbing-image nudged elastic band method [45]. To identify the most stable adsorption sites of Li^+ on three surfaces, multiple possible adsorption sites on three surfaces were considered (Fig. 2b and Fig. S3). It is shown that the $Al_{\text{-top-L1}}$ site on $Li_2Al(110)$, $Li_{\text{-top-L2}}$ on Li(001) and $F_{\text{-top}}$ site on LiF(001) are the most stable positions for the adsorbed Li^+ with adsorption energies of 1.99, 1.50 and 0.44 eV, respectively. Then, the two most stable positions of Li^+ on the three surfaces were selected as the initial and final sites for calculating the diffusion energy barrier of Li^+. As presented in Fig 2c and Fig. S4, the energy barrier of Li^+ diffusion on the Li_2Al (110) surface is 0.02 eV, much lower than those on the LiF(001) surface (0.18 eV) and Li(001) surface (0.05 eV), which will facilitate Li^+ transfer through the SEI and promote uniform Li deposition.

Although lithiophilic Li-Al alloys can help enhance the interfacial contact and regulate the Li deposition, their electron-conducting nature render them inapt as the SEI layer [37,46]. As shown in Fig. 2d, the electrons in Li metal will spontaneously transfer to the SEI side due to the internal electric field driven by the higher energy (lower work function) of the electron in Li metal, which will accelerate Li dendrite growth and side reactions at the interface. Therefore, a satisfactory SEI is required to be electron-insulating. In this regard, the LiF-rich SEI layer will play a role due to the strong electron-blocking nature of LiF. The electron blocking effect

of LiF is first verified by macro-average electrostatic potential profiles (Fig. 2d). The difference between the electrostatic potentials (approximately the Fermi level of the component on each side of the interface, represented by dashed lines) determines the strength of the internal electric field. It can be observed that the difference of LiF(001)/Li(110) (4.47 eV) is much larger than that in the Li_2Al(110)/Li(110) interface (2.83 eV), implying that the barrier of electron tunneling into the SEI is larger at the LiF(001)/Li(001) interface. The band structure calculation also indicates that the LiF exhibits a huge bandgap of 8.89 eV to block the electron transfer, whereas Li_2Al exhibits a metallic property (Fig. S5). Additionally, Bader charge analysis verifies that 0.14 electrons/per atom transfer from the Li metal part to the Li_2Al part, which is much higher than that occurring at the Li/LiF interface (0.02 electrons per Li atom). Furthermore, the ability for electron transfer from Li to two components was directly calculated from the density of states (DOS) profiles by taking the difference of the conduction band minimum and Fermi level (0 eV). As shown in Fig. 2e, the second atomic layer of Li_2Al still exhibits a high electron-conducting property, making them fail to block the electron migration from the Li metal to the inner part. In contrast, the electron tunneling barrier between Li metal and LiF is over 2 eV at layer 2, indicating the high electron-blocking effect of LiF. In addition to the electron-insulating nature, LiF possesses high lithiophobicity and bulk modulus (62.61 GPa, Table S2), which will help prevent the Li propagation and penetration into the solid electrolyte and minimize SEI deformation associated with volume change, thereby stabilizing the interface [30,39]. These results indicate that the combination of the Li-Al alloy-rich layer and LiF-rich layer would be promising to overcome the challenge of undesirable Li plating/stripping behavior existing in PEO-based solid batteries.

Furthermore, to verify the experimental feasibility of in-situ forming lithiophilic-lithiophobic SEI layers, we further calculated the reduction and oxidation energy levels of the $Al(OTF)_3$, LiTFSI and PEO. As shown in Fig. 2f, the lowest unoccupied molecular orbital

(LUMO) levels of the three components show an increased trend by -1.86, -1.19 and -0.69 eV, respectively, indicating that the Al salt will be preferentially reduced by Li metal anode to form a Li-Al alloy-rich layer. Moreover, the LUMO levels of LiF and Li_2Al are 7.75 and 3.96 eV, respectively, which are much higher than the LUMO calculated for any other basic components in the coating layer, demonstrating this gradient SEI layer possesses good stability against Li metal once formed, which is also consistent with the phase diagram of Li-Al-F (Fig. S1).

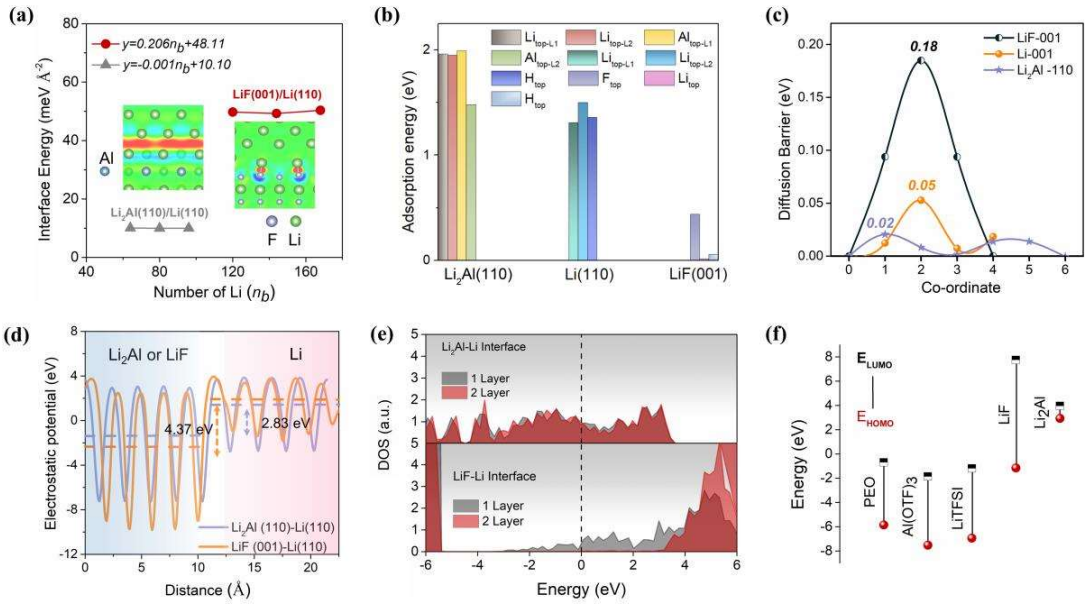

Fig. 2 (a) Plots of the relationship between the interface energy for Li_2Al and LiF components and the number of Li metal formula units. The inset images are 2D cross-sectional charge density difference of $Li_2Al(110)/Li(110)$ (left) and LiF(001)/Li(110) (right) interfaces. The iso-surface level is 0.002 e $Å^{-3}$. (b) Adsorption energies for different Li^+ adsorption sites on Li_2Al (110), Li (001) and LiF (001) surfaces. (c) Diffusion energy barriers of Li^+ on the LiF(001), $Li_2Al(110)$ and Li(001) surfaces. (d) Electrostatic potential profiles of $Li_2Al(110)/Li(110)$ and LiF(001)/Li(110) interfaces. (e) DOS of $Li_2Al(110)/Li(110)$ and LiF(001)/Li(110) interfaces. (f) Computed reduction and oxidation energy levels of PEO, LiTFSI, $Al(OTF)_3$, Li_2Al, and LiF.

2.2 Characterizations of the modified Li/PEO interface

In this work, PVDF fiber network-supported PEO/LiTFSI electrolyte (denoted as FPEO) is used due to its higher ionic conductivity, mechanical strength and processability compared to its pure PEO/LiTFSI counterpart [9]. The detailed information of the FPEO electrolyte can be found in Supporting Information (Fig. S6 & 7). A thin layer containing Al/Li dual-salt and PEO was directly coated on the FPEO electrolyte, then the targeted interphases will be obtained upon cycling. Fig. 3a shows the cross-sectional image of the dual-salt coated FPEO electrolyte. The thickness of the FPEO electrolyte was measured to be about 35 μm. No obvious boundary can be detected, indicating good adhesion between the coating layer and the bulk FPEO electrolyte. The top view (Fig. 3b) reveals that the surface of the dual-salt coated FPEO electrolytes is smooth and uniform. The inset EDX mapping shows the homogeneous distribution of Al and F signals. This is conducive to interface stability. The time-of-flight secondary ion mass spectrometry (TOF-SIMS) test in positive mode was performed to determine the thickness of the dual-salt coating layer (Fig. S8). As evidenced by the Al^+ signal distribution, the thickness of the dual-salt coating layer is determined to be around 350 nm, which is sufficient for forming the targeted SEI without sacrificing the ion conduction of the electrolyte.

The electrochemical behaviour of the Al/Li dual-salt coated electrolyte was first investigated by the cyclic voltammetry (CV) test of Li/Cu cells. As shown in Fig. 3c, the cell with $Al(OTF)_3$/LiTFSI dual-salt coating exhibits an additional reduction peak at around 0.7 V vs. Li^+/Li, in comparison to those containing either LiTFSI or LiOTF single salt, which can be ascribed to the pre-deposition of Al, consistent with our computational result [47,48]. Moreover, the CV curve of the Al/Li dual-salt cell exhibits a smaller Li deposition overpotential and larger peak current, indicating the formation of Li-Al alloy with a smaller diffusion barrier for Li^+ can help promote Li deposition. The voltage profiles of the Cu/Li batteries at a plating current density of 0.1 mA cm^{-2} for 10 h is shown in Fig. 3d. Benefiting from the lithiophilic Li-Al

alloying-rich layer, the coating of a dual-salt layer reduces the nucleation overpotential of Li on the Cu current collector from 96 to 49 mV. More importantly, the incorporation of Al salt allows Li to stably deposit for 10 h without short circuits, while the cell without Al salt gets short-circuited after around 4-h deposition due to the dendrite penetration. These experimental results demonstrate that the coating of Al/Li dual salt layer can effectively decrease of the Li plating resistance and induce the homogenous Li deposition.

To optimize the salt concentration and evaluate the stability of the Li metal anode/solid electrolyte interface, Li/Li symmetrical cells were assembled with various weight ratio of the LiTFSI/$Al(OTF)_3$ dual-salt (i.e., 4:0, 3:2, 2:3, 1:4) and a fixed weight ratio of PEO/total salt (10:5). As shown in Fig. S9, without (single Li salt) or with a small portion of Al salt (Li:Al = 3:2), the cells get short-circuited rapidly due to severe Li dendrite growth as a result of the poor interfacial adhesion and large interface overpotential. When the Li-Al ratio is increased to 2:3, the cell can be stably cycled at 0.1, 0.2 and 0.3 mA cm^{-2}, indicating its good rate performance and stability. However, further increasing the Al content to a Li/Al ratio of 1:4, the cell overpotential increases due to the lack of mobile Li^+ in the coating layer [49]. Additionally, the cell shows poorer cycle stability, indicating that too much Al salt may deteriorate the interface. This might be because that the $TFSI^-$ anions can lead to a better LiF-rich SEI layer compared to its OTF^- counterpart. To prove this hypothesis, we retrieved the Li metal anode cycled in the cell with the coating layer containing the same weight of LiOTF and LiTFSI salt and analysed the surface properties via X-ray photoelectron spectroscopy (XPS). As shown in Fig. S10, the LiF signal of cycled Li metal anode with LiTFSI coating layer is much stronger than that with LiOTF, suggesting that the $TFSI^-$ is more beneficial for forming a LiF-rich SEI layer. As shown in Fig. 3f, the symmetric cell with the optimized Li/Al ratio of 2:3 displays an outstanding cycling performance for another 1000 h when the current density returns to 0.1 mA cm^{-2}. Therefore, Li/Al ratio of 2:3 is chosen for the following characterizations.

The impedance evolution of symmetric cells cycling at 0.1 mA cm^{-2} was evaluated by electrochemical impedance spectroscopy (EIS) tests. As shown in Fig. 3f, in the absence of Al salt, the cell exhibits a large resistance of 871 and 1007 Ω after 10-h and 100-h cycling, respectively, and then gets short-circuited (Fig. S11). In contrast, with optimal Al/Li dual-salt coating, the impedance of the cell is considerably reduced to 242 Ω, and shows negligible increase even after cycling for 500 h (Fig. 3g), indicative of improved Li^+ transfer across the interface and remarkable interface stability. Moreover, with the dual-salt coating layer, the cell can even be cycled at an areal capacity of 1 mAh cm^{-2}, in sharp contrast to quick shorting of its counterpart (Fig. 3h). In addition, the critical current density (CCD) of the FPEO electrolyte can be improved from 1.0 to 1.7 mA cm^{-2} in the presence of dual-salt coating layer (Fig. 3i). These encouraging results demonstrate that our strategy can effectively improve the stability of Li/polymer electrolyte interface.

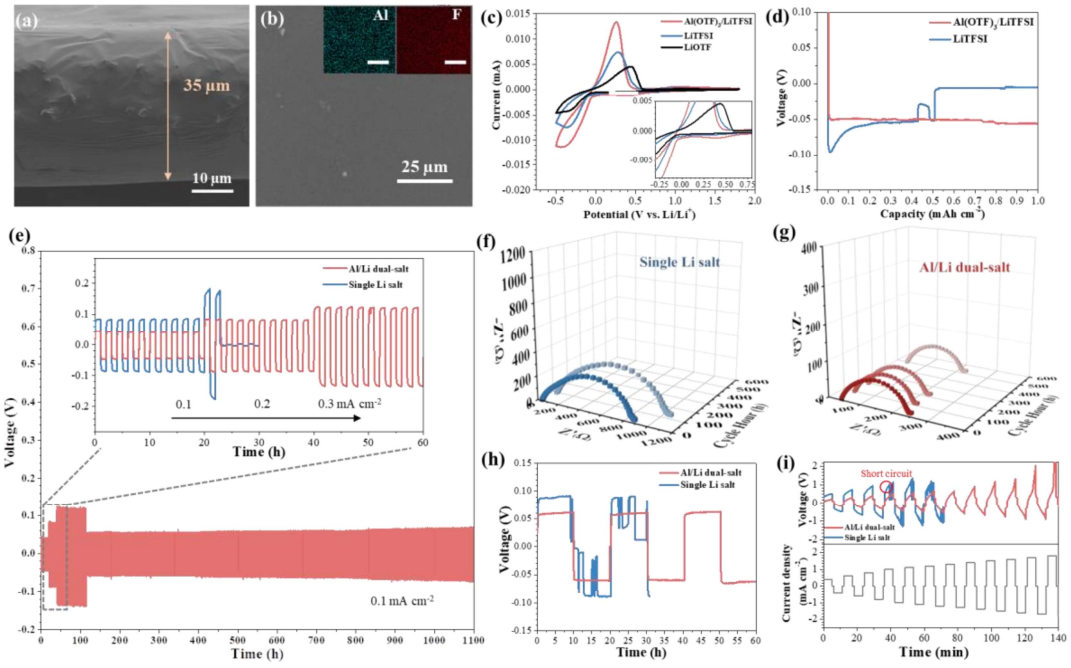

Fig. 3 SEM images of the (a) cross-sectional view and (b) front view of the FPEO electrolyte with the dual-salt coating layer. The inset in b is the EDX mapping of Al and F elements. (c) CV tests of Li/Cu cells using FPEO electrolytes with coating layers containing different salts.

(d) Li plating profiles on the Cu working electrode at 0.1 mA cm^{-1} and 1 mAh cm^{-2}. (e) Cycling performance of Li/Li symmetrical cells at 55 °C at 2-h plating/stripping periods. Inset in e shows the enlarged cycling profile of the first 60 h. Nyquist plots of cell with coating layer containing (f) single Li salt, and (g) Al/Li dual-salt. (h) Galvanostatic cycling of cells at a current density of 0.1 mA cm^{-2} under a fixed areal capacity of 1 mAh cm^{-2}. (i) Critical current density tests with a stripping/plating period of 10 min.

To reveal the origin of the superior performance of the symmetric cell with Al/Li dual-salt coating layer, the Li metal surface and Li/polymer interface were characterized after cycling at 0.1 mA cm^{-2} for 50 h. As shown in Fig. 4a, the cycled Li metal surface retrieved from the cell with single Li salt coating layer shows a dendritic and rough morphology. In addition, voids and detachment are clearly observed at the Li/FPEO electrolyte interface (Fig. 4b), indicating the poor interface adhesion. In sharp contrast, with the dual-salt coating layer, the cycled Li metal surface remains smooth without obvious dendrite formation (Fig. 4c). Moreover, Fig. 4d shows that the FPEO electrolyte closely adheres to the Li metal even after cycling, confirming that the addition of the Al salt can indeed endow the interface with good adhesion, thereby alleviating the Li dendrite formation.

Depth-profiling XPS and TOF-SIMS tests were further conducted to elucidate the SEI composition of the Li metal surface cycled with the dual-salt coating layer. Fig. 4e and f show the XPS spectra at increasing sputtering time of F 1s and Al 2p signals, respectively. As shown in Fig. 4e, the peak at 688.9 eV stems from the residual Li salt on the Li metal surface, which disappears upon sputtering. The peak at 685.1 eV can be ascribed to the LiF due to the reduction of salts. The intensity of the LiF signal first increases with sputtering time, and then decreases, indicating that the LiF-rich layer is located at the top of SEI (close to the electrolyte). As shown in Fig. 4f, the peak of Al^{3+} (77.8 eV) at the surface might result from the residual Al salt and

Al_2O_3 formed during sample transfer, which also disappears upon sputtering. The peaks located at 75.8, 72.9 and 70.0 eV can be ascribed to Li_xAlO_y, $Li_{1-x}Al$ and $Li_{1+x}Al$ species, respectively, which originates from the reduction of Al cations and the following lithiation reactions [50]. The intensity of Li-Al alloy peaks increases upon sputtering, indicating that the alloy-rich layer is located at the bottom of SEI (close to the anode). TOF-SIMS top-down depth profiles and their corresponding 3D renderings are presented in Fig. 4g-i. LiF_2^- and Al^- are selected to represent the LiF and Li-Al alloy, respectively, which are the primary components of the lithiophobic-lithiophilic SEI species. As shown in Fig. 4g, the LiF_2^- signal intensity remains high on the surface layer and decreases after 100 s of Cs^+ sputtering, while the Al^- increases at first and reaches highest at 200 s. The transition from the LiF-rich layer to Li-Al alloy-rich layer can be clearly demonstrated in the corresponding 3D renderings (Fig. 4h and i), which is constant with the XPS results. These results verify the successful formation of lithiophilic-lithiophobic gradient SEI layer, which dramatically improves the stability of the Li/electrolyte interface.

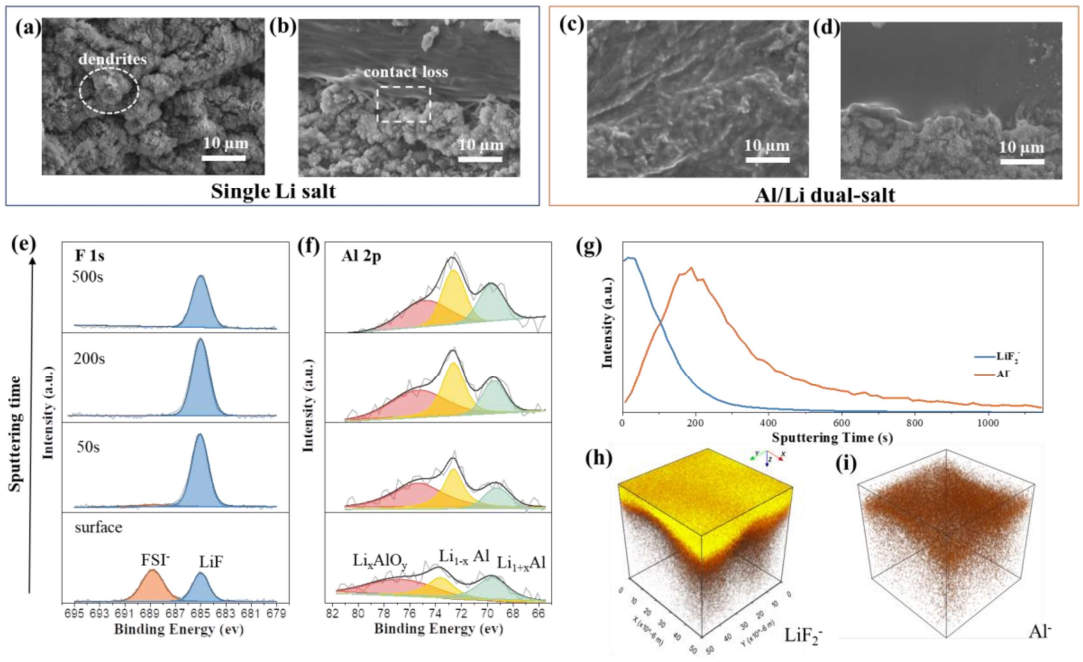

Fig. 4 Characterizations of the Li/electrolyte interface after cycling in Li/Li symmetric cells for 50 h at 0.1 mA cm^{-2}. SEM images of the Li metal surface from the cells (a) with single Li salt, and (c) Al/Li dual-salt. SEM images of the cross-sectional view of the Li/electrolyte interface from the cells (b) with single Li salt, and (d) Al/Li dual-salt. XPS spectra at different sputtering time of (e) F 1s and (f) Al 2p of Li metal surface from the cell with dual-salt coating layer. (g) TOF-SIMS depth profiles of the SEI layer from the cell with Al/Li dual-salt coating layer, wherein LiF_2^- and Al^- were selected to represent LiF and Li-Al alloys, respectively. (h, i) 3D visual renderings of the TOF-SIMS depth profiles presented in (g).

2.3 Evaluation of full battery performance

To demonstrate the pratical application of the dual-salt coated electrolyte, full cells paired with $LiFePO_4$ (LFP) cathode were assembled and evaluated through galvanostatic charge/discharge at 55 °C. As shown in Fig. 5a, the cell with dual-salt coating is capable of delivering high capacities of 163.9, 155.0, 148.9, and 135.5 mAh g^{-1} at 0.1, 0.3, 0.5 and 1 C, respectively. When the current returns to 0.5 C, the cell can still maintain a capacity of 145.6 mAh g^{-1}. Fig. 5b displays the charge/discharge curves of the Li/LFP full cell with dual-salt coating. Typical charge-discharge voltage plateaus can be observed even at 1 C. The Nyquist plots of Li/$LiFePO_4$ cells with different coating are shown in Fig. S12. It can be found the cell with single Li salt coating shows a large impedance, which may be due to the lithiophobic nature of LiF-rich SEI that compromises the contact between the Li and PEO. As a consequence, the cell with single Li salt coating delivers much lower capacities and Coulombic efficiencies at 0.1 and 0.3 C, which even gets short-circuited at 0.5 C (Fig. 5a). By comparison, benefiting from the enhanced interface contact induced by lithiophihic Li-Al alloys, the cell with dual-salt coating shows a smaller resistance at the anode interface. Meanwhile, the lithiophobic LiF layer formed near the PEO electrolyte side contributes to the dendrite suppression. As a result, the

cell with dual-salt coating achieves outstanding cycling performance, retaining 89.1% of its initial capacity after 350 cycles at 0.5 C (Fig. 5c). In sharp contrast, the cell with single Li salt can only be cycled for 20 cycles at 0.5 C. These results imply that the lithiophobic LiF-rich interphase alone cannot prevent dendrite formation, leading to short life of the battery. By adding Al salt, the resultant lithiophilic-lithiophobic gradient interphase can improve the interfacial contact and suppress dendrite formation, thus greatly extending the cycle life of the full battery.

Encouraged by the outstanding battery performance in coin cell configuration, an all-solid-state pouch cell with a cathode loading of 4.0 mg cm^{-2} was assembled to demonstrate its potential for large-scale applications. As shown in Fig. 5d and Fig. S13, the pouch cell exhibits typical charge-discharge curves and delivers a high capacity of 150.2 mAh g^{-1} (0.60 mAh cm^{-2}) at 0.1 C. Impressively, the pouch cell can still power a LED when folded and after cutting, demonstrating its excellent tolerability toward abusive testing conditions and superior safety.

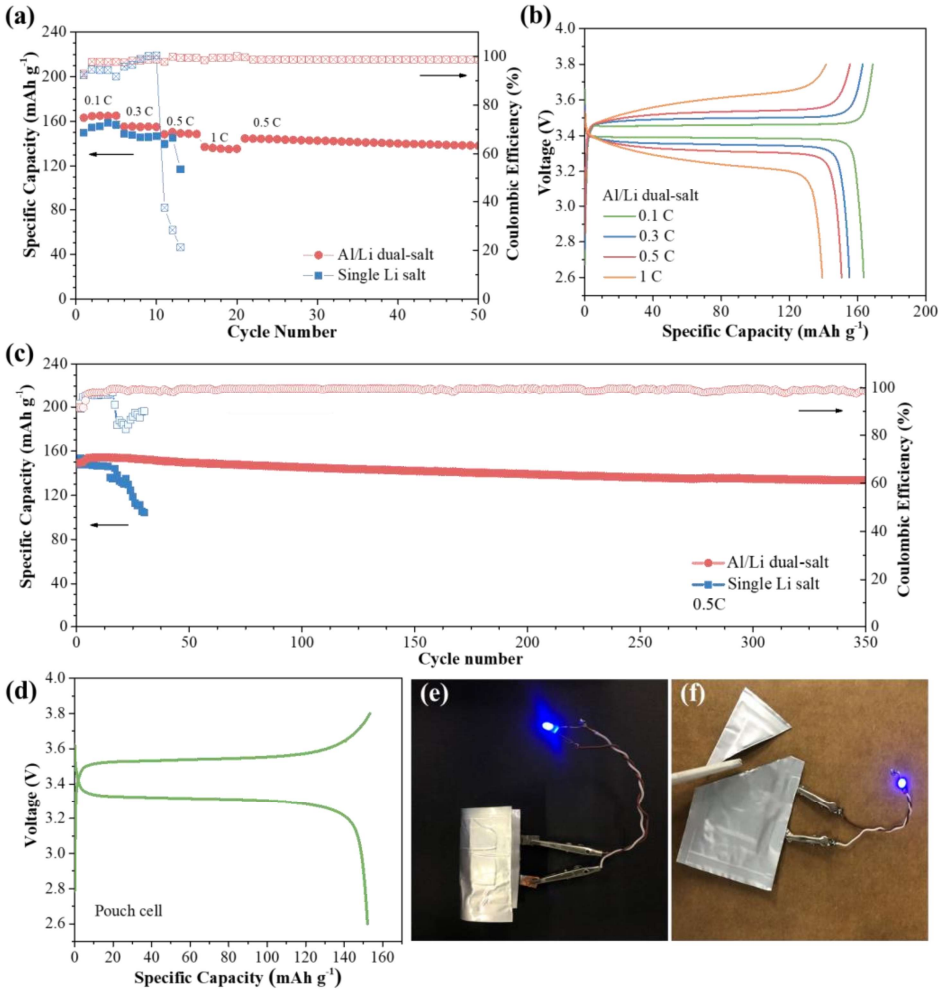

Fig. 5 Electrochemical performance of ASSLBs using $LiFePO_4$ cathode at 55 °C. (a) Rate performance of the cells with Al/Li dual-salt and single Li salt coating layer. (b) Voltage profiles at different C rates of the cell with dual-salt coating layer. (c) Cycling performance of cells with Al/Li dual-salt and single Li salt coating layer at 0.5 C. (d) Voltage profile of the pouch cell at 0.1 C. Photographs of pouch cells powering a LED (e) when bending and (f) after cutting.

3. Conclusion

In summary, an in-situ formed lithiophilic-lithiophobic gradient SEI layer is successfully developed to simultaneously improve the interface adhesion and suppress the Li dendrite by

simply coating the PEO-based electrolyte with an Al/Li dual-salt layer. A lithiophilic Li-Al alloy-rich layer is obtained near the Li anode to improve the interface adhesion and regulate the Li nucleation; while a lithiophobic LiF-rich layer is formed close to the electrolyte side to offer high interface energy for dendrite suppression. As a result, the Li/Li symmetrical cell with the dual-salt coated electrolyte can be stably cycled for over 1000 h without short circuits. Moreover, the coated polymer electrolyte enables the Li/$LiFePO_4$ full cell to stably operate at 0.5 C with capacity retention of 89.1% after 350 cycles. Additionally, the pouch cell demonstrates a good performance and survives from blending and cutting, showing great promise for practical applications. These results demonstrate that our approach can effectively improve the anode stability in a facile way, opening a new avenue for highly stable ASSLBs employing SPEs.

4. Experiments

4.1 Fabrication of FPEO electrolytes with coating layer

The PVDF fiber framework, which was employed as the support to improve the mechanical properties of the PEO electrolyte, was prepared by electrospinning technique developed in our previous works [9]. To prepare the FPEO electrolytes, the PEO (Mw = 600,000) and LiTFSI (2:1 by weight) were first dissolved in acetonitrile (ACN) to get a homogenous solution, followed by infusing this solution into the electronspun PVDF fiber network and drying under vacuum at 60 °C for about 24 h.

PEO and a certain amount of LiTFSI and $Al(OTF)_3$ were dissolved in ACN to obtain the coating layer slurry, wherein the weight ratio of the PEO over salts was fixed at 2:1. The slurry was then directly cast on the surface FPEO electrolyte, forming a thin coating layer after drying at 60 °C for over 24 h in a vacuum.

4.2 Electrochemical characterizations

The CV test was conducted on Biologic SP 300 at a voltage range from 1.8 to -0.5 V with a scan rate of 0.1 mV s^{-1}. The EIS tests were conducted on a potentiostat (Biologic, SP 300) in the frequency range from 7 M to 1 Hz with an amplitude of 10 mV.

To prepare the LFP cathode, the $LiFePO_4$ powders (MTI Co.), PEO, LiTFSI, and Supper P (MTI Co.) were mixed in ACN at a weight ratio 80:8:2:10. The slurry was vigorously stirred for 12 h and cast on a carbon-coated Al foil, followed by drying at 65 °C overnight in a vacuum oven and calendaring. The cathode loading is weighed to be around 3.6 mg cm^{-2}. An integrated cathode/FPEO configuration developed in our previous work was adopted for full battery assembly, wherein the FPEO electrolyte is directly fabricated on the prepared cathode, followed by coating the dual-salt layer upon it [9]. 2032 coin cells were assembled by stacking Li metal and the integrated cathode/FPEO for battery tests. The pouch cell with a size of 3.5 × 4 cm^2 and a cathode loading of 4 mg cm^{-2} was assembled in a similar way with coin cells. All batteries were assembled in an argon-filled glovebox with O_2 and H_2O contents below 0.1 ppm, and were tested on a battery cycling system (Neware, CT-3008W) at 55 °C.

4.3 Material characterizations

Scanning electron microscopy (SEM) images were obtained on a JEOL-7100 instrument. X-ray photoelectron spectroscopy (XPS) was conducted on a Physical Electronics PHI 5600 multi-technique system using an Al monochromatic X-ray source at 350 W. The time-of-flight secondary ion mass spectrometry (ToF-SIMS) was carried out on a TOF SIMS V (ION-TOF GmbH) instrument equipped with a primary beam of Bi ion source and sputtering beams of Cs and Ar ion source for negative and positive mode respectively.

4.4 DFT calculations

All the computational simulations were performed on basis of density functional theory (DFT) calculations with a plane-wave technique which is implemented in the Vienna ab initio simulation package (VASP) [51,52]. Gradient corrected exchange-correlation functional of

Perdew, Burke, and Ernzerhof (PBE) models were used under the projector augmented wave (PAW) method [53,54], with cut-off kinetic energy of 520 eV for plane wave basis. The convergence criterion of the total energy was set up to be within 1×10^{-5} eV, while all the atoms and geometries were optimized until the residual forces became less than 1×10^{-2} eV Å^{-1}. For Li, LiF and Li_2Al crystals, these optimized energetically most favorable structures after the full geometry relaxation were implemented within a K-point 11 × 11 × 11, 9 × 9 × 9 and 9 × 9 × 10 grid, respectively. For all the surface-related calculations including the adsorption of atoms and diffusion energy barrier of Li^+ on the Li (001), Li_2Al (110) and LiF (001) surfaces, they were carried out within a K-point 2 × 2 × 1 grid. In the vertical direction, a vacuum layer of 15 Å thick was introduced for all surfaces. Transition states of Li^+ diffusion and kinetic barriers were determined by the CI-NEB method [55].

Acknowledgement

The work described in this paper was fully supported by a grant from the Research Grants Council of the Hong Kong Special Administrative Region, China (Project No. R6005-20).

Conflicts of interest

The authors declare no conflict of interest.

References

[1] J. Liu, Z. Bao, Y. Cui, E.J. Dufek, J.B. Goodenough, P. Khalifah, Q. Li, B.Y. Liaw, P. Liu, A. Manthiram, Y.S. Meng, V.R. Subramanian, M.F. Toney, V. V. Viswanathan, M.S. Whittingham, J. Xiao, W. Xu, J. Yang, X.-Q. Yang, J.-G. Zhang, Pathways for practical high-energy long-cycling lithium metal batteries, Nat. Energy. 4 (2019) 180–186.

[2] C. Zhao, G.-L. Xu, Z. Yu, L. Zhang, I. Hwang, Y.-X. Mo, Y. Ren, L. Cheng, C.-J.

Sun, Y. Ren, X. Zuo, J.-T. Li, S.-G. Sun, K. Amine, T. Zhao, A high-energy and long-cycling lithium–sulfur pouch cell via a macroporous catalytic cathode with double-end binding sites, Nat. Nanotechnol. 16 (2021) 166–173.

[3] D. Lin, Y. Liu, Y. Cui, Reviving the lithium metal anode for high-energy batteries, Nat. Nanotechnol. 12 (2017) 194–206.

[4] J. Wan, J. Xie, X. Kong, Z. Liu, K. Liu, F. Shi, A. Pei, H. Chen, W. Chen, J. Chen, X. Zhang, L. Zong, J. Wang, L.-Q. Chen, J. Qin, Y. Cui, Ultrathin, flexible, solid polymer composite electrolyte enabled with aligned nanoporous host for lithium batteries, Nat. Nanotechnol. 14 (2019) 705–711.

[5] X. Peng, Y. Lin, Y. Wang, Y. Li, T. Zhao, A lightweight localized high-concentration ether electrolyte for high-voltage Li-Ion and Li-metal batteries, Nano Energy. 96 (2022) 107102.

[6] S. Randau, D.A. Weber, O. Kötz, R. Koerver, P. Braun, A. Weber, E. Ivers-Tiffée, T. Adermann, J. Kulisch, W.G. Zeier, F.H. Richter, J. Janek, Benchmarking the performance of all-solid-state lithium batteries, Nat. Energy. 5 (2020) 259–270.

[7] T. Famprikis, P. Canepa, J.A. Dawson, M.S. Islam, C. Masquelier, Fundamentals of inorganic solid-state electrolytes for batteries, Nat. Mater. 18 (2019) 1278–1291.

[8] Y. Xiao, K. Turcheniuk, A. Narla, A.-Y. Song, X. Ren, A. Magasinski, A. Jain, S. Huang, H. Lee, G. Yushin, Electrolyte melt infiltration for scalable manufacturing of inorganic all-solid-state lithium-ion batteries, Nat. Mater. 20 (2021) 984–990.

[9] Y. Lin, M. Wu, J. Sun, L. Zhang, Q. Jian, T. Zhao, A High- Capacity, Long- Cycling All- Solid- State Lithium Battery Enabled by Integrated Cathode/Ultrathin Solid Electrolyte, Adv. Energy Mater. 11 (2021) 2101612.

[10] Y.-G. Lee, S. Fujiki, C. Jung, N. Suzuki, N. Yashiro, R. Omoda, D.-S. Ko, T. Shiratsuchi, T. Sugimoto, S. Ryu, J.H. Ku, T. Watanabe, Y. Park, Y. Aihara, D. Im,

I.T. Han, High-energy long-cycling all-solid-state lithium metal batteries enabled by silver–carbon composite anodes, Nat. Energy. 5 (2020) 299–308.

[11] Y. Lin, K. Liu, M. Wu, C. Zhao, T. Zhao, Enabling Solid-State Li Metal Batteries by In Situ Forming Ionogel Interlayers, ACS Appl. Energy Mater. 3 (2020) 5712–5721.

[12] Y. Ren, Z. Cui, A. Bhargav, J. He, A. Manthiram, A Self-Healable Sulfide/Polymer Composite Electrolyte for Long-Life, Low-Lithium-Excess Lithium-Metal Batteries, Adv. Funct. Mater. 32 (2021) 2106680.

[13] J. Zhang, C. Zheng, L. Li, Y. Xia, H. Huang, Y. Gan, C. Liang, X. He, X. Tao, W. Zhang, Unraveling the Intra and Intercycle Interfacial Evolution of Li6PS5Cl-Based All-Solid-State Lithium Batteries, Adv. Energy Mater. 10 (2020) 1–12.

[14] Z. Zou, Y. Li, Z. Lu, D. Wang, Y. Cui, B. Guo, Y. Li, X. Liang, J. Feng, H. Li, C.-W. Nan, M. Armand, L. Chen, K. Xu, S. Shi, Mobile Ions in Composite Solids, Chem. Rev. 120 (2020) 4169–4221.

[15] Z. Li, H. Zhang, X. Sun, Y. Yang, Mitigating Interfacial Instability in Polymer Electrolyte-Based Solid-State Lithium Metal Batteries with 4 v Cathodes, ACS Energy Lett. 5 (2020) 3244–3253.

[16] X. Yang, M. Jiang, X. Gao, D. Bao, Q. Sun, N. Holmes, H. Duan, S. Mukherjee, K. Adair, C. Zhao, J. Liang, W. Li, J. Li, Y. Liu, H. Huang, L. Zhang, S. Lu, Q. Lu, R. Li, C.V. Singh, X. Sun, Determining the limiting factor of the electrochemical stability window for PEO-based solid polymer electrolytes: main chain or terminal –OH group?, Energy Environ. Sci. 13 (2020) 1318–1325.

[17] J. Zhang, C. Zheng, J. Lou, Y. Xia, C. Liang, H. Huang, Y. Gan, X. Tao, W. Zhang, Poly(ethylene oxide) reinforced Li6PS5Cl composite solid electrolyte for all-solid-state lithium battery: Enhanced electrochemical performance, mechanical property and interfacial stability, J. Power Sources. 412 (2019) 78–85.

[18] C. Wang, T. Yang, W. Zhang, H. Huang, Y. Gan, Y. Xia, X. He, J. Zhang, Hydrogen bonding enhanced SiO2/PEO composite electrolytes for solid-state lithium batteries, J. Mater. Chem. A. 10 (2022) 3400–3408.

[19] P. Yao, B. Zhu, H. Zhai, X. Liao, Y. Zhu, W. Xu, Q. Cheng, C. Jayyosi, Z. Li, J. Zhu, K.M. Myers, X. Chen, Y. Yang, PVDF/Palygorskite Nanowire Composite Electrolyte for 4 v Rechargeable Lithium Batteries with High Energy Density, Nano Lett. 18 (2018) 6113–6120.

[20] K. Liu, M. Wu, H. Jiang, Y. Lin, T. Zhao, An ultrathin, strong, flexible composite solid electrolyte for high-voltage lithium metal batteries, J. Mater. Chem. A. 8 (2020) 18802–18809.

[21] N. Wu, P.H. Chien, Y. Li, A. Dolocan, H. Xu, B. Xu, N.S. Grundish, H. Jin, Y.Y. Hu, J.B. Goodenough, Fast Li+ Conduction Mechanism and Interfacial Chemistry of a NASICON/Polymer Composite Electrolyte, J. Am. Chem. Soc. 142 (2020) 2497–2505.

[22] W.P. Chen, H. Duan, J.L. Shi, Y. Qian, J. Wan, X.D. Zhang, H. Sheng, B. Guan, R. Wen, Y.X. Yin, S. Xin, Y.G. Guo, L.J. Wan, Bridging Interparticle Li+Conduction in a Soft Ceramic Oxide Electrolyte, J. Am. Chem. Soc. 143 (2021) 5717–5726.

[23] O. Sheng, C. Jin, M. Chen, Z. Ju, Y. Liu, Y. Wang, J. Nai, T. Liu, W. Zhang, X. Tao, Platinum nano-interlayer enhanced interface for stable all-solid-state batteries observed: Via cryo-transmission electron microscopy, J. Mater. Chem. A. 8 (2020) 13541–13547.

[24] H. Duan, M. Fan, W. Chen, J. Li, P. Wang, W. Wang, J. Shi, Y. Yin, L. Wan, Y. Guo, Extended Electrochemical Window of Solid Electrolytes via Heterogeneous Multilayered Structure for High- Voltage Lithium Metal Batteries, Adv. Mater. 31 (2019) 1807789.

[25] B. Xu, X. Li, C. Yang, Y. Li, N.S. Grundish, P. Chien, K. Dong, I. Manke, R. Fang, N. Wu, H. Xu, A. Dolocan, J.B. Goodenough, Interfacial Chemistry Enables Stable Cycling of All-Solid-State Li Metal Batteries at High Current Densities, J. Am. Chem. Soc. 143 (2021) 6542–6550.

[26] G. Wang, P. He, L. Fan, Asymmetric Polymer Electrolyte Constructed by Metal–Organic Framework for Solid- State, Dendrite- Free Lithium Metal Battery, Adv. Funct. Mater. 31 (2021) 2007198.

[27] Y. Lin, K. Liu, C. Xiong, M. Wu, T. Zhao, A composite solid electrolyte with an asymmetric ceramic framework for dendrite-free all-solid-state Li metal batteries, J. Mater. Chem. A. 9 (2021) 9665–9674.

[28] O. Sheng, J. Zheng, Z. Ju, C. Jin, Y. Wang, M. Chen, J. Nai, T. Liu, W. Zhang, Y. Liu, X. Tao, In Situ Construction of a LiF- Enriched Interface for Stable All- Solid- State Batteries and its Origin Revealed by Cryo- TEM, Adv. Mater. 32 (2020) 2000223.

[29] H. Huo, Y. Chen, J. Luo, X. Yang, X. Guo, X. Sun, Rational Design of Hierarchical "Ceramic- in- Polymer" and "Polymer- in- Ceramic" Electrolytes for Dendrite- Free Solid- State Batteries, Adv. Energy Mater. 9 (2019) 1804004.

[30] X. Ji, S. Hou, P. Wang, X. He, N. Piao, J. Chen, X. Fan, C. Wang, Solid- State Electrolyte Design for Lithium Dendrite Suppression, Adv. Mater. 32 (2020) 2002741.

[31] J. Kasemchainan, S. Zekoll, D. Spencer Jolly, Z. Ning, G.O. Hartley, J. Marrow, P.G. Bruce, Critical stripping current leads to dendrite formation on plating in lithium anode solid electrolyte cells, Nat. Mater. 18 (2019) 1105–1111.

[32] X. Fan, X. Ji, F. Han, J. Yue, J. Chen, L. Chen, T. Deng, J. Jiang, C. Wang, Fluorinated solid electrolyte interphase enables highly reversible solid-state Li metal battery, Sci. Adv. 4 (2018) eaau9245.

[33] L. Ye, X. Li, A dynamic stability design strategy for lithium metal solid state batteries,

Nature. 593 (2021) 218–222.

[34] D.H.S. Tan, Y.-T. Chen, H. Yang, W. Bao, B. Sreenarayanan, J. Doux, W. Li, B. Lu, S. Ham, B. Sayahpour, J. Scharf, E.A. Wu, G. Deysher, H.E. Han, H.J. Hah, H. Jeong, J.B. Lee, Z. Chen, Y.S. Meng, Carbon-free high-loading silicon anodes enabled by sulfide solid electrolytes, Science (80-.). 373 (2021) 1494–1499.

[35] W. Luo, Y. Gong, Y. Zhu, Y. Li, Y. Yao, Y. Zhang, K.K. Fu, G. Pastel, C. Lin, Y. Mo, E.D. Wachsman, L. Hu, Reducing Interfacial Resistance between Garnet- Structured Solid- State Electrolyte and Li- Metal Anode by a Germanium Layer, Adv. Mater. 29 (2017) 1606042.

[36] X. Han, Y. Gong, K.K. Fu, X. He, G.T. Hitz, J. Dai, A. Pearse, B. Liu, H. Wang, G. Rubloff, Negating interfacial impedance in garnet-based solid-state Li metal batteries, Nat. Mater. 16 (2017) 572.

[37] T. Wang, J. Duan, B. Zhang, W. Luo, X. Ji, H. Xu, Y. Huang, L. Huang, Z. Song, J. Wen, C. Wang, Y. Huang, J.B. Goodenough, A self-regulated gradient interphase for dendrite-free solid-state Li batteries, Energy Environ. Sci. 15 (2022) 1325–1333.

[38] A. Mirsakiyeva, M. Ebadi, C.M. Araujo, D. Brandell, P. Broqvist, J. Kullgren, Initial Steps in PEO Decomposition on a Li Metal Electrode, J. Phys. Chem. C. 123 (2019) 22851–22857.

[39] J. Chen, Q. Li, T.P. Pollard, X. Fan, O. Borodin, C. Wang, Electrolyte design for Li metal-free Li batteries, Mater. Today. 39 (2020) 118–126.

[40] R. Weber, M. Genovese, A.J. Louli, S. Hames, C. Martin, I.G. Hill, J.R. Dahn, Long cycle life and dendrite-free lithium morphology in anode-free lithium pouch cells enabled by a dual-salt liquid electrolyte, Nat. Energy. 4 (2019) 683–689.

[41] Z. Tu, M.J. Zachman, S. Choudhury, K.A. Khan, Q. Zhao, L.F. Kourkoutis, L.A. Archer, Stabilizing Protic and Aprotic Liquid Electrolytes at High-Bandgap Oxide

Interphases, Chem. Mater. 30 (2018) 5655–5662.

[42] B.S. Vishnugopi, F. Hao, A. Verma, L.E. Marbella, V. Viswanathan, P.P. Mukherjee, Co-Electrodeposition Mechanism in Rechargeable Metal Batteries, ACS Energy Lett. 6 (2021) 2190–2197.

[43] S.H. Lee, J. Hwang, J. Ming, Z. Cao, H.A. Nguyen, H. Jung, J. Kim, Y. Sun, Toward the Sustainable Lithium Metal Batteries with a New Electrolyte Solvation Chemistry, Adv. Energy Mater. 10 (2020) 2000567.

[44] N.D. Lepley, N.A.W. Holzwarth, Modeling interfaces between solids: Application to Li battery materials, Phys. Rev. B. 92 (2015) 214201.

[45] A. Hu, W. Chen, X. Du, Y. Hu, T. Lei, H. Wang, L. Xue, Y. Li, H. Sun, Y. Yan, J. Long, C. Shu, J. Zhu, B. Li, X. Wang, J. Xiong, An artificial hybrid interphase for an ultrahigh-rate and practical lithium metal anode, Energy Environ. Sci. 14 (2021) 4115–4124.

[46] X.B. Cheng, C.Z. Zhao, Y.X. Yao, H. Liu, Q. Zhang, Recent Advances in Energy Chemistry between Solid-State Electrolyte and Safe Lithium-Metal Anodes, Chem. 5 (2019) 74–96.

[47] M. Shimizu, M. Umeki, S. Arai, Suppressing the effect of lithium dendritic growth by the addition of magnesium bis(trifluoromethanesulfonyl)amide, Phys. Chem. Chem. Phys. 20 (2018) 1127–1133.

[48] L. Cao, D. Li, F.A. Soto, V. Ponce, B. Zhang, L. Ma, T. Deng, J.M. Seminario, E. Hu, X. Yang, P.B. Balbuena, C. Wang, Highly Reversible Aqueous Zinc Batteries enabled by Zincophilic–Zincophobic Interfacial Layers and Interrupted Hydrogen- Bond Electrolytes, Angew. Chemie Int. Ed. 60 (2021) 18845–18851.

[49] H. Wan, S. Liu, T. Deng, J. Xu, J. Zhang, X. He, X. Ji, X. Yao, C. Wang, Bifunctional Interphase-Enabled Li 10 GeP 2 S 12 Electrolytes for Lithium–Sulfur Battery, ACS

Energy Lett. 6 (2021) 862–868.

[50] B. Qin, T. Diemant, H. Zhang, A. Hoefling, R.J. Behm, J. Tübke, A. Varzi, S. Passerini, Revisiting the Electrochemical Lithiation Mechanism of Aluminum and the Role of Li-rich Phases (Li1+xAl) on Capacity Fading, ChemSusChem. 12 (2019) 2609–2619.

[51] G. Kresse, J. Furthmüller, Efficient iterative schemes for ab initio total-energy calculations using a plane-wave basis set, Phys. Rev. B. 54 (1996) 11169–11186.

[52] G. Kresse, J. Furthmüller, Efficiency of ab-initio total energy calculations for metals and semiconductors using a plane-wave basis set, Comput. Mater. Sci. 6 (1996) 15–50.

[53] P.E. Blöchl, Projector augmented-wave method, Phys. Rev. B. 50 (1994) 17953–17979.

[54] G. Kresse, D. Joubert, From ultrasoft pseudopotentials to the projector augmented-wave method, Phys. Rev. B. 59 (1999) 1758–1775.

[55] G. Henkelman, B.P. Uberuaga, H. Jónsson, A climbing image nudged elastic band method for finding saddle points and minimum energy paths, J. Chem. Phys. 113 (2000) 9901–9904.